Spectroscopy and Cross Sections of Near-Drip Line N=28 Aluminum and Island of Inversion Neon Produced by Nucleon Knockout Reactions

MURRAY Ian

Institut de Physique Nucléaire d'Orsay

Driving forces of shell (*and magic number*) evolution

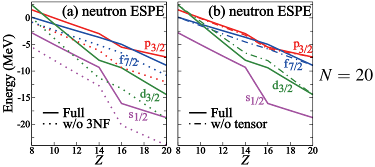

Theoretical effective single particle (orbital) energies for $N = 20$ isotones. Figure from Tsunoda et al. 2017.

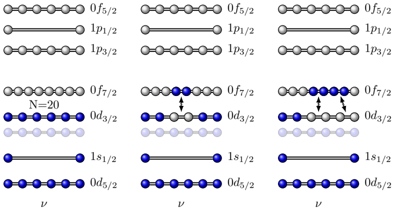

0p-0h 2p-2h 4p-4h

So-called *normal* and *intruder* neutron configurations

Tensor component of the monopole part of the NN interaction

- Monopole part of the tensor force between proton and neutrons and spin-orbit coupling partners: $j_> = \ell + s$ and $j_< = \ell - s$
- Energy Splitting: $(2j_> + 1)V^{tensor}_{j_>j'} + (2j_< + 1)V^{tensor}_{j_<j'} = 0$

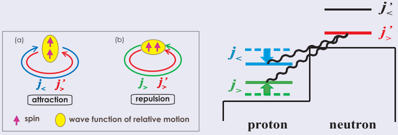

Graphics from Otsuka et al. 2005

Intruders and correlations

- $N = 20$ Island of inversion: multiparticle/hole (such as 2p-2h) configurations energetically favored to take over the ground state
- Intruder states highly correlated to compensate for the energy loss from unnatural filling
- Smaller shell gap easier to overcome

Island of Inversion $N = 20$

$N = 20$

$^{30}_{14}\mathbf{Si}_{16}$	$^{31}_{14}\mathrm{Si}_{17}$	$^{32}_{14}\mathbf{Si}_{18}$	$^{33}_{14}\mathrm{Si}_{19}$	$^{34}_{14}\mathbf{Si}_{20}$	$^{35}_{14}\mathrm{Si}_{21}$	$^{36}_{14}\mathbf{Si}_{22}$	$^{37}_{14}\mathrm{Si}_{23}$	$^{38}_{14}\mathbf{Si}_{24}$
$^{29}_{13}\mathrm{Al}_{16}$	$^{30}_{13}\mathrm{Al}_{17}$	$^{31}_{13}\mathrm{Al}_{18}$	$^{32}_{13}\mathrm{Al}_{19}$	$^{33}_{13}\mathrm{Al}_{20}$	$^{34}_{13}\mathrm{Al}_{21}$	$^{35}_{13}\mathrm{Al}_{22}$	$^{36}_{13}\mathrm{Al}_{23}$	$^{37}_{13}\mathrm{Al}_{24}$
$^{28}_{12}\mathbf{Mg}_{16}$	$^{29}_{12}\mathrm{Mg}_{17}$	$^{30}_{12}\mathbf{Mg}_{18}$	$^{31}_{12}\mathrm{Mg}_{19}$	$^{32}_{12}\mathbf{Mg}_{20}$	$^{33}_{12}\mathrm{Mg}_{21}$	$^{34}_{12}\mathbf{Mg}_{22}$	$^{35}_{12}\mathrm{Mg}_{23}$	$^{36}_{12}\mathbf{Mg}_{24}$
$^{27}_{11}\mathrm{Na}_{16}$	$^{28}_{11}\mathrm{Na}_{17}$	$^{29}_{11}\mathrm{Na}_{18}$	$^{30}_{11}\mathrm{Na}_{19}$	$^{31}_{11}\mathrm{Na}_{20}$	$^{32}_{11}\mathrm{Na}_{21}$	$^{33}_{11}\mathrm{Na}_{22}$	$^{34}_{11}\mathrm{Na}_{23}$	$^{35}_{11}\mathrm{Na}_{24}$
$^{26}_{10}\mathbf{Ne}_{16}$	$^{27}_{10}\mathrm{Ne}_{17}$	$^{28}_{10}\mathbf{Ne}_{18}$	$^{29}_{10}\mathrm{Ne}_{19}$	$^{30}_{10}\mathbf{Ne}_{20}$	$^{31}_{10}\mathrm{Ne}_{21}$	$^{32}_{10}\mathbf{Ne}_{22}$	$^{33}_{10}\mathrm{Ne}_{23}$	$^{34}_{10}\mathrm{Ne}_{24}$

- Consider only isotopes with even numbers of protons and neutrons

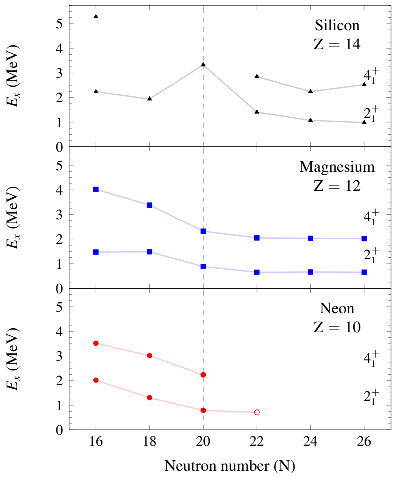

Horizontal bars are shell model calculations with EKK developed *sdpf* effective interaction Tsunoda et al. 2017. Experimental data from Basunia 2010; Basunia and Hurst 2016; Doornenbal et al. 2013; Nica, Cameron, and Singh 2012; Nica and Singh 2012; Shamsuzzoha Basunia 2013; Takeuchi et al. 2012.

Island of Inversion $N = 20$

				$N = 20$				
${}^{30}_{14}\mathrm{Si}_{16}$	${}^{31}_{14}\mathrm{Si}_{17}$	${}^{32}_{14}\mathrm{Si}_{18}$	${}^{33}_{14}\mathrm{Si}_{19}$	${}^{34}_{14}\mathrm{Si}_{20}$	${}^{35}_{14}\mathrm{Si}_{21}$	${}^{36}_{14}\mathrm{Si}_{22}$	${}^{37}_{14}\mathrm{Si}_{23}$	${}^{38}_{14}\mathrm{Si}_{24}$
${}^{29}_{13}\mathrm{Al}_{16}$	${}^{30}_{13}\mathrm{Al}_{17}$	${}^{31}_{13}\mathrm{Al}_{18}$	${}^{32}_{13}\mathrm{Al}_{19}$	${}^{33}_{13}\mathrm{Al}_{20}$	${}^{34}_{13}\mathrm{Al}_{21}$	${}^{35}_{13}\mathrm{Al}_{22}$	${}^{36}_{13}\mathrm{Al}_{23}$	${}^{37}_{13}\mathrm{Al}_{24}$
${}^{28}_{12}\mathrm{Mg}_{16}$	${}^{29}_{12}\mathrm{Mg}_{17}$	${}^{30}_{12}\mathrm{Mg}_{18}$	${}^{31}_{12}\mathrm{Mg}_{19}$	${}^{32}_{12}\mathrm{Mg}_{20}$	${}^{33}_{12}\mathrm{Mg}_{21}$	${}^{34}_{12}\mathrm{Mg}_{22}$	${}^{35}_{12}\mathrm{Mg}_{23}$	${}^{36}_{12}\mathrm{Mg}_{24}$
${}^{27}_{11}\mathrm{Na}_{16}$	${}^{28}_{11}\mathrm{Na}_{17}$	${}^{29}_{11}\mathrm{Na}_{18}$	${}^{30}_{11}\mathrm{Na}_{19}$	${}^{31}_{11}\mathrm{Na}_{20}$	${}^{32}_{11}\mathrm{Na}_{21}$	${}^{33}_{11}\mathrm{Na}_{22}$	${}^{34}_{11}\mathrm{Na}_{23}$	${}^{35}_{11}\mathrm{Na}_{24}$
${}^{26}_{10}\mathrm{Ne}_{16}$	${}^{27}_{10}\mathrm{Ne}_{17}$	${}^{28}_{10}\mathrm{Ne}_{18}$	${}^{29}_{10}\mathrm{Ne}_{19}$	${}^{30}_{10}\mathrm{Ne}_{20}$	${}^{31}_{10}\mathrm{Ne}_{21}$	${}^{32}_{10}\mathrm{Ne}_{22}$	${}^{33}_{10}\mathrm{Ne}_{23}$	${}^{34}_{10}\mathrm{Ne}_{24}$

- So-called *island of inversion* $\approx Z \leq 12$ and $N \geq 20$
- From spherical to prolate deformation in Mg to Ne
- Presently understood as a *large area of deformation*

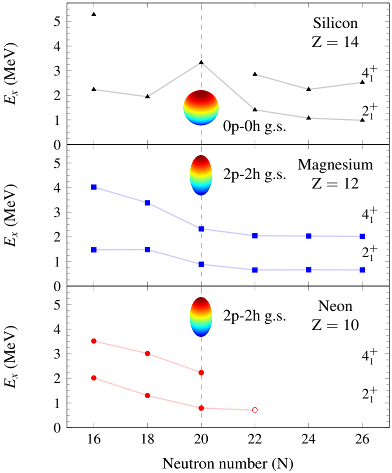

Horizontal bars are shell model calculations with EKK developed *sdpf* effective interaction Tsunoda et al. 2017. Experimental data from Basunia 2010; Basunia and Hurst 2016; Doornenbal et al. 2013; Nica, Cameron, and Singh 2012; Nica and Singh 2012; Shamsuzzoha Basunia 2013; Takeuchi et al. 2012.

In-beam γ-ray spectroscopy to reveal exited state nuclear structure

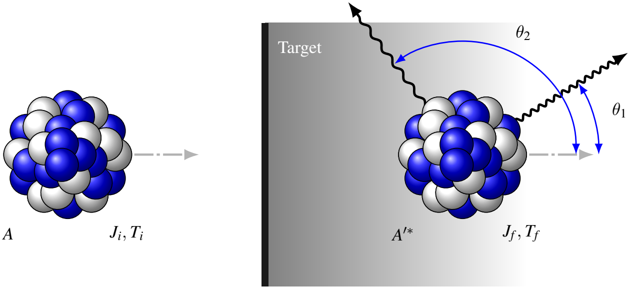

- Nuclear reactions of fast ion-beams with targets $\rightarrow$ appreciable probability to populate nuclear excited states of the reaction residue
- De-excitation of states observed in motion (ion-beam)
  - Doppler shift at relativistic ion-beam energy

RIKEN Nishina Center for Accelerator-Based Science

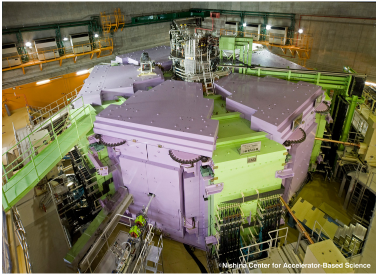

Superconducting Ring Cyclotron (SRC)

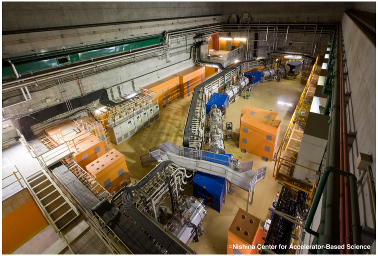

BigRIPS fragment separator

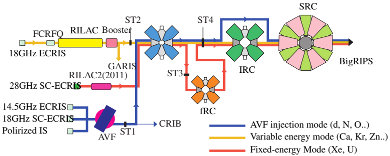

Overview of the RIBF accelerators Okuno, Fukunishi, and Kamigaito 2012.

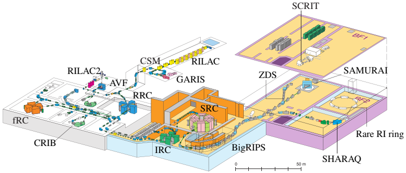

RIKEN Nishina Center Okuno, Fukunishi, and Kamigaito 2012.

Overview of BigRIPS separator, ZeroDegree spectrometer, beamline detectors and DALI

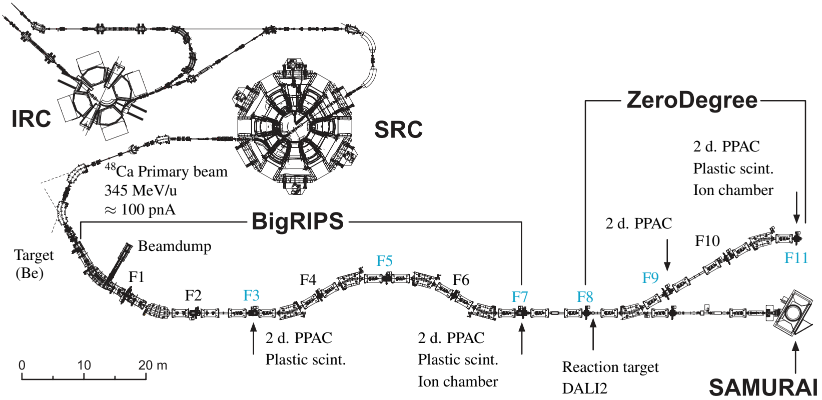

Overview of the IRC, SRC accelerators and the BigRIPS separator and ZeroDegree spectrometer. Image from Kubo et al. 2012.

- RIKEN BigRIPS separator and ZeroDegree spectrometer, in combination with beamline detectors acts as a kind of *filter* to select a reaction channel
- Projectiles (before reaction target) and reaction residues (after reacterion target) are selected in data analysis

Overview of BigRIPS separator, ZeroDegree spectrometer, beamline detectors and DALI

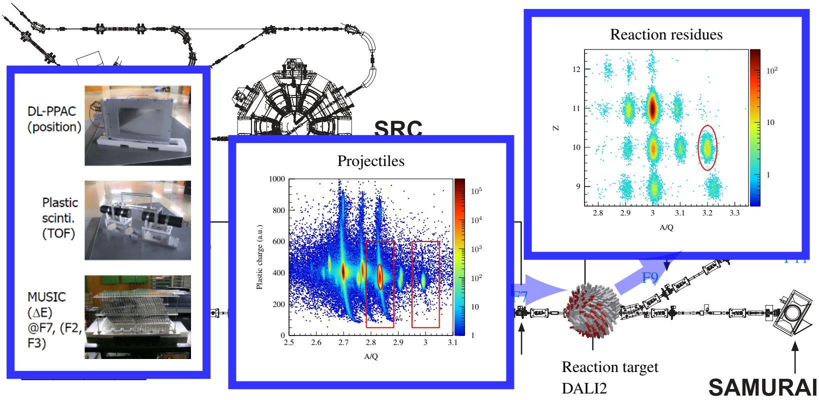

Overview of the IRC, SRC accelerators and the BigRIPS separator and ZeroDegree spectrometer. Image from Kubo et al. 2012.

- RIKEN BigRIPS separator and ZeroDegree spectrometer, in combination with beamline detectors acts as a kind of *filter* to select a reaction channel
- Projectiles (before reaction target) and reaction residues (after reacterion target) are selected in data analysis

Overview of BigRIPS separator, ZeroDegree spectrometer, beamline detectors and DALI

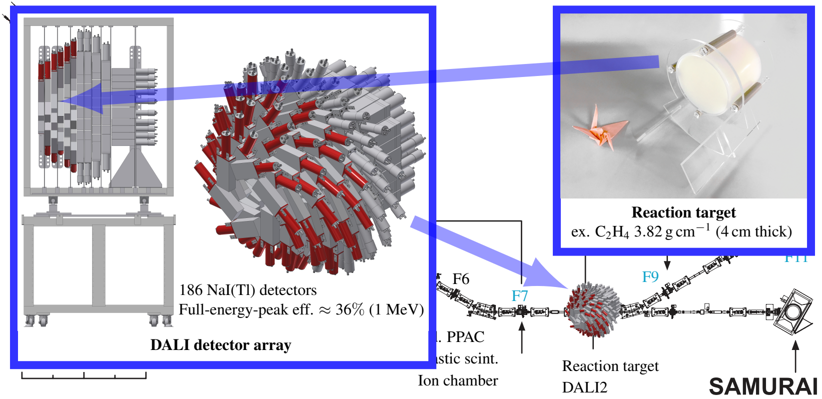

Overview of the IRC, SRC accelerators and the BigRIPS separator and ZeroDegree spectrometer. Image from Kubo et al. 2012.

- RIKEN BigRIPS separator and ZeroDegree spectrometer, in combination with beamline detectors acts as a kind of *filter* to select a reaction channel
- Projectiles (before reaction target) and reaction residues (after reacterion target) are selected in data analysis
- DALI2 detector arrays surrounds reaction target to observe prompt gamma-rays

^{34}Mg(^{9}Be,X)^{32}Ne

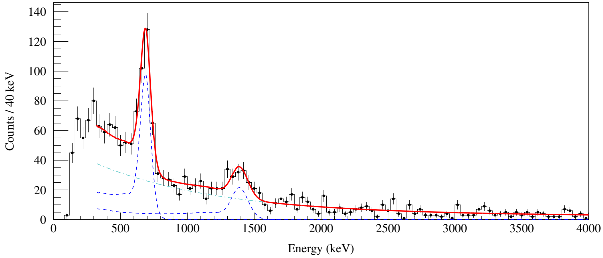

Fit of ^{34}Mg(^{9}Be,X)^{32}Ne doppler reconstructed γ-ray energy spectrum, $m_\gamma \leq 3$, and with add-back

Table: Two-proton knockout

E_γ (keV)	Yield/100 ions
$708(5)_{stat.}$	33(3)
$1405(19)_{stat.}$	17(3)

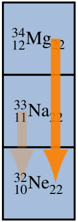

- Peak around 700 keV previously identified and interpreted as $2^+_1 \rightarrow 0^+_{g.s.}$ transition
- New transition observed around 1400 keV in 2-proton knockout

^{33}Na(^{9}Be,X)^{32}Ne

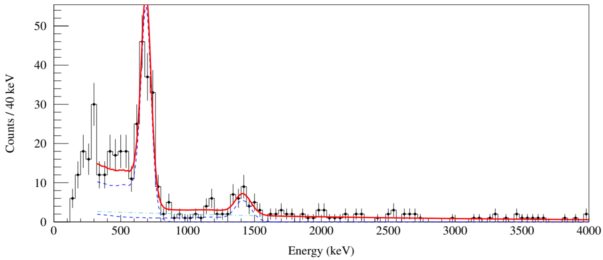

Fit of ^{33}Na(^{9}Be,X)^{32}Ne doppler reconstructed γ-ray energy spectrum, $m_\gamma \leq 3$, and with add-back

Table: One-proton knockout

E_γ (keV)	Yield/100 ions
$710(5)_{stat.}$	72(7)
$1415(21)_{stat.}$	17(5)

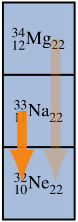

- Peak around 700 keV previously identified and interpreted as $2^+_1 \rightarrow 0^+_{g.s.}$ transition
- New transition observed around 1400 keV in 2-proton knockout and 1-proton knockout

... and γ-γ coincidence

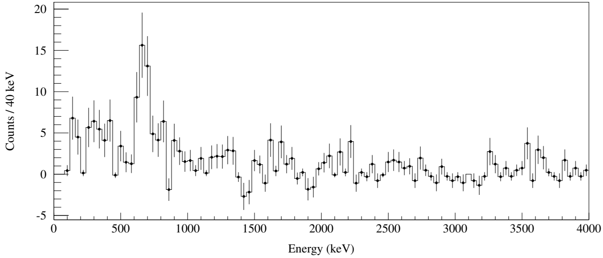

Background subtracted coincidences for 1410(15) keV (1300 keV to 1500 keV), combined -2 & -1p, all m_γ

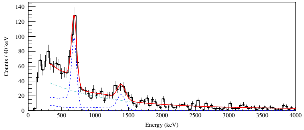

^{34}Mg(^{9}Be,X)^{32}Ne

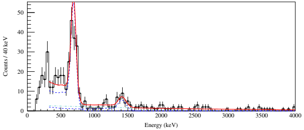

^{33}Na(^{9}Be,X)^{32}Ne

- 1410(15) keV coincident with 709(12) keV with relative intensity of 108(20) %
- Suggests two transitions as part of cascade
- Consistent with interpretation of $4^+ \to 2^+$ transition
  - systematics, comparison to theoretical exclusive cross sections, low S_n ...

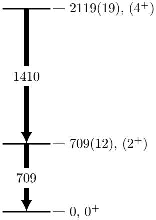

Comparison with shell model predictions

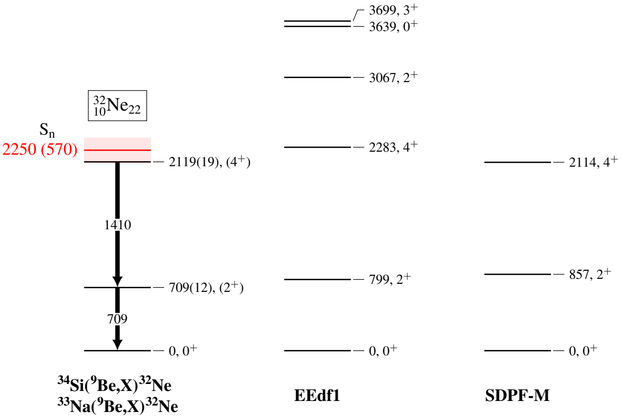

- Good agreement with predicted $E(4_1^+)$ and $E(2_1^+)$
- No other levels below extrapolated neutron separation energy to compete with transition assignments
- Experimental $R_{4/2}$ ratio of 2.99 close to (and larger than) predicted 2.86, 2.45 by SM calculations

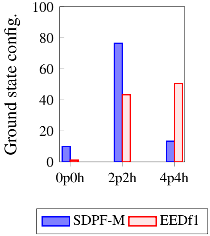

Interpretation of $E(4_1^+)$

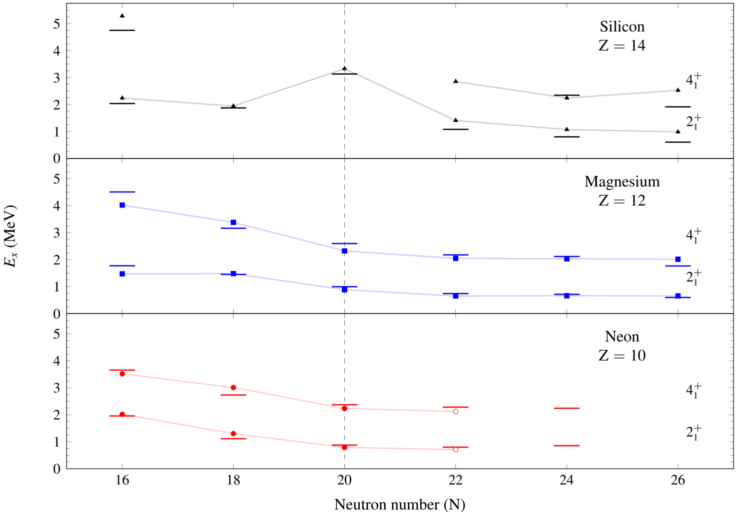

Horizontal bars are shell model calculations with EKK developed *sdpf* effective interaction Tsunoda et al. 2017. Experimental data from Nuclear data sheets and Doornenbal et al. 2013; Nica, Cameron, and Singh 2012; Takeuchi et al. 2012.

Interpretation of $E(4_1^+)$

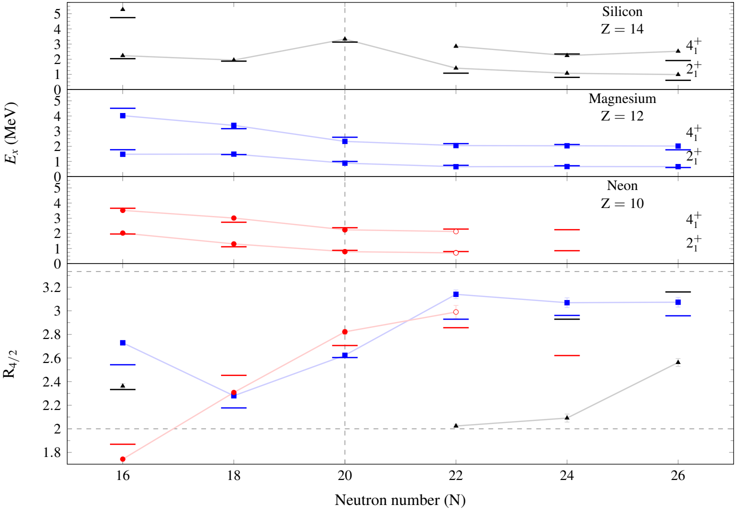

Horizontal bars are shell model calculations with EKK developed *sdpf* effective interaction Tsunoda et al. 2017. Experimental data from Nuclear data sheets and Doornenbal et al. 2013; Nica, Cameron, and Singh 2012; Takeuchi et al. 2012.

Interpretation of $E(4^+_1)$

$N = 20$

$^{30}_{14}Si_{16}$	$^{31}_{14}Si_{17}$	$^{32}_{14}Si_{18}$	$^{33}_{14}Si_{19}$	$^{34}_{14}Si_{20}$	$^{35}_{14}Si_{21}$	$^{36}_{14}Si_{22}$	$^{37}_{14}Si_{23}$	$^{38}_{14}Si_{24}$
$^{29}_{13}Al_{16}$	$^{30}_{13}Al_{17}$	$^{31}_{13}Al_{18}$	$^{32}_{13}Al_{19}$	$^{33}_{13}Al_{20}$	$^{34}_{13}Al_{21}$	$^{35}_{13}Al_{22}$	$^{36}_{13}Al_{23}$	$^{37}_{13}Al_{24}$
$^{28}_{12}Mg_{16}$	$^{29}_{12}Mg_{17}$	$^{30}_{12}Mg_{18}$	$^{31}_{12}Mg_{19}$	$^{32}_{12}Mg_{20}$	$^{33}_{12}Mg_{21}$	$^{34}_{12}Mg_{22}$	$^{35}_{12}Mg_{23}$	$^{36}_{12}Mg_{24}$
$^{27}_{11}Na_{16}$	$^{28}_{11}Na_{17}$	$^{29}_{11}Na_{18}$	$^{30}_{11}Na_{19}$	$^{31}_{11}Na_{20}$	$^{32}_{11}Na_{21}$	$^{33}_{11}Na_{22}$	$^{34}_{11}Na_{23}$	$^{35}_{11}Na_{24}$
$^{26}_{10}Ne_{16}$	$^{27}_{10}Ne_{17}$	$^{28}_{10}Ne_{18}$	$^{29}_{10}Ne_{19}$	$^{30}_{10}Ne_{20}$	$^{31}_{10}Ne_{21}$	$^{32}_{10}\mathbf{Ne}_{22}$	$^{33}_{10}Ne_{23}$	$^{34}_{10}Ne_{24}$

Interpretation of $E(4_1^+)$

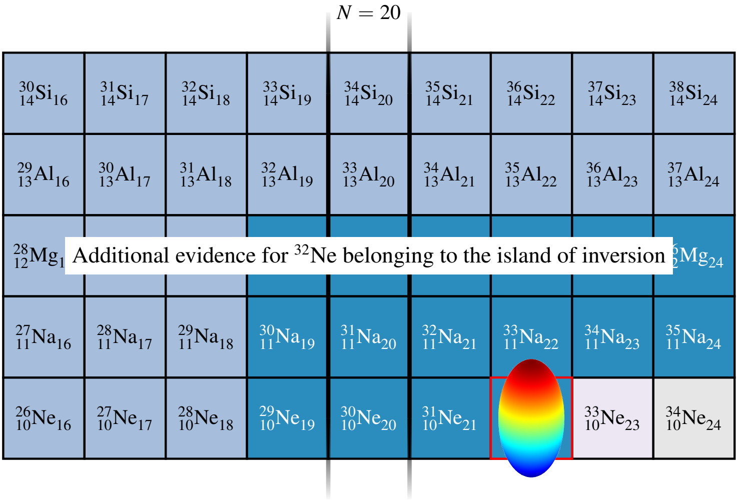

Additional evidence for ^{32}Ne belonging to the island of inversion

Interpretation of one and two-nucleon knockout cross sections

One proton knockout cross section ratio

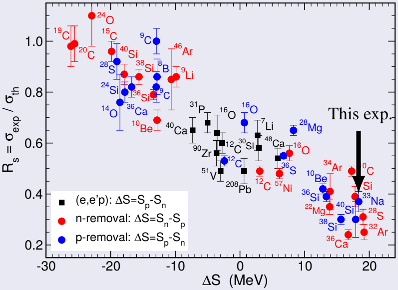

Private communication by Jeff Tostevin

- Nucleon separation asymmetry of ^{33}Na: $\Delta S = S_{proton} - S_{neutron} = +18.37$ MeV
- Nuclear structure and reaction theory cannot be disentangled to explain trend

Two proton knockout cross section ratio

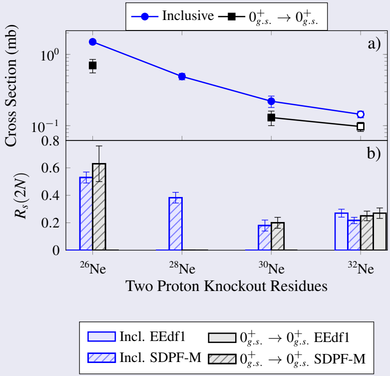

Data taken from Bazin et al. 2003; Fallon et al. 2010; Tostevin and Brown 2006

- Limited trend in neutron-rich Neon isotopes
- Similarity between EEdf1 and SDPF-M shell model interactions (similar two-nucleon amplitudes (TNAs))

Neutron number $N = 28$

$N = 20$								$N = 28$
$^{37}_{17}Cl_{20}$	$^{38}_{17}Cl_{21}$	$^{39}_{17}Cl_{22}$	$^{40}_{17}Cl_{23}$	$^{41}_{17}Cl_{24}$	$^{42}_{17}Cl_{25}$	$^{43}_{17}Cl_{26}$	$^{44}_{17}Cl_{27}$	$^{45}_{17}Cl_{28}$
$^{36}_{16}S_{20}$	$^{37}_{16}S_{21}$	$^{38}_{16}S_{22}$	$^{39}_{16}S_{23}$	$^{40}_{16}S_{24}$	$^{41}_{16}S_{25}$	$^{42}_{16}S_{26}$	$^{43}_{16}S_{27}$	$^{44}_{16}S_{28}$
$^{35}_{15}P_{20}$	$^{36}_{15}P_{21}$	$^{37}_{15}P_{22}$	$^{38}_{15}P_{23}$	$^{39}_{15}P_{24}$	$^{40}_{15}P_{25}$	$^{41}_{15}P_{26}$	$^{42}_{15}P_{27}$	$^{43}_{15}P_{28}$
$^{34}_{14}Si_{20}$	$^{35}_{14}Si_{21}$	$^{36}_{14}Si_{22}$	$^{37}_{14}Si_{23}$	$^{38}_{14}Si_{24}$	$^{39}_{14}Si_{25}$	$^{40}_{14}Si_{26}$	$^{41}_{14}Si_{27}$	$^{42}_{14}Si_{28}$
$^{33}_{13}Al_{20}$	$^{34}_{13}Al_{21}$	$^{35}_{13}Al_{22}$	$^{36}_{13}Al_{23}$	$^{37}_{13}Al_{24}$	$^{38}_{13}Al_{25}$	$^{39}_{13}\mathbf{Al}_{26}$	$^{40}_{13}\mathbf{Al}_{27}$	$^{41}_{13}\mathbf{Al}_{28}$
$^{32}_{12}Mg_{20}$	$^{33}_{12}Mg_{21}$	$^{34}_{12}Mg_{22}$	$^{35}_{12}Mg_{23}$	$^{36}_{12}Mg_{24}$	$^{37}_{12}Mg_{25}$	$^{38}_{12}Mg_{26}$	$^{39}_{12}Mg_{27}$	$^{40}_{12}Mg_{28}$

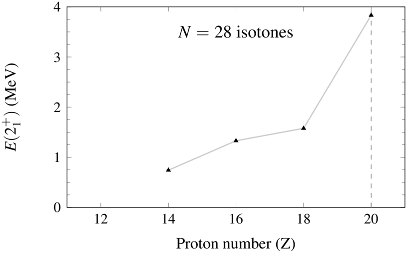

- Ex: observed with decreasing $E(2^+_1)$ energy

Neutron number $N = 28$

$N = 20$								$N = 28$
$^{37}_{17}$Cl$_{20}$	$^{38}_{17}$Cl$_{21}$	$^{39}_{17}$Cl$_{22}$	$^{40}_{17}$Cl$_{23}$	$^{41}_{17}$Cl$_{24}$	$^{42}_{17}$Cl$_{25}$	$^{43}_{17}$Cl$_{26}$	$^{44}_{17}$Cl$_{27}$	$^{45}_{17}$Cl$_{28}$
$^{36}_{16}$S$_{20}$	$^{37}_{16}$S$_{21}$	$^{38}_{16}$S$_{22}$	$^{39}_{16}$S$_{23}$	$^{40}_{16}$S$_{24}$	$^{41}_{16}$S$_{25}$	$^{42}_{16}$S$_{26}$	$^{43}_{16}$S$_{27}$	$^{44}_{16}$S$_{28}$
$^{35}_{15}$P$_{20}$	$^{36}_{15}$P$_{21}$	$^{37}_{15}$P$_{22}$	$^{38}_{15}$P$_{23}$	$^{39}_{15}$P$_{24}$	$^{40}_{15}$P$_{25}$	$^{41}_{15}$P$_{26}$	$^{42}_{15}$P$_{27}$	$^{43}_{15}$P$_{28}$
$^{34}_{14}$Si$_{20}$	$^{35}_{14}$Si$_{21}$	$^{36}_{14}$Si$_{22}$	$^{37}_{14}$Si$_{23}$	$^{38}_{14}$Si$_{24}$	$^{39}_{14}$Si$_{25}$	$^{40}_{14}$Si$_{26}$	$^{41}_{14}$Si$_{27}$	$^{42}_{14}$Si$_{28}$
$^{33}_{13}$Al$_{20}$	$^{34}_{13}$Al$_{21}$	$^{35}_{13}$Al$_{22}$	$^{36}_{13}$Al$_{23}$	$^{37}_{13}$Al$_{24}$	$^{38}_{13}$Al$_{25}$	$^{39}_{13}$**Al**$_{26}$	$^{40}_{13}$**Al**$_{27}$	$^{41}_{13}$**Al**$_{28}$
$^{32}_{12}$Mg$_{20}$	$^{33}_{12}$Mg$_{21}$	$^{34}_{12}$Mg$_{22}$	$^{35}_{12}$Mg$_{23}$	$^{36}_{12}$Mg$_{24}$	$^{37}_{12}$Mg$_{25}$	$^{38}_{12}$Mg$_{26}$	$^{39}_{12}$Mg$_{27}$	$^{40}_{12}$Mg$_{28}$

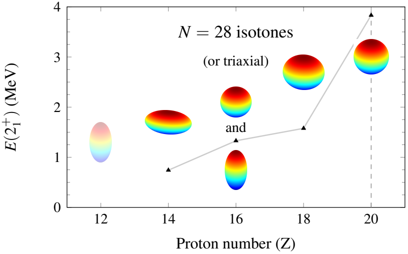

- Ex: observed with decreasing $E(2_1^+)$ energy
- Evolution of deformation from spherical ^{48}Ca $\rightarrow$ oblate ^{42}Si
- Removal of $\pi 0d_{3/2}$ protons $\Rightarrow \downarrow$ spiting of $\nu 0f_{5/2}$ and $\nu 0f_{7/2}$
- Jahn-Teller effect (near degeneracy of orbits) favours deformation
- $\Delta j = 2$ with occupied and valence proton/neutron orbitals $\Rightarrow$ cross-shell quadrupole excitations (SU(3) symmetries of Elliott)

Neutron number $N = 28$

$N = 20$								$N = 28$
$^{37}_{17}$Cl$_{20}$	$^{38}_{17}$Cl$_{21}$	$^{39}_{17}$Cl$_{22}$	$^{40}_{17}$Cl$_{23}$	$^{41}_{17}$Cl$_{24}$	$^{42}_{17}$Cl$_{25}$	$^{43}_{17}$Cl$_{26}$	$^{44}_{17}$Cl$_{27}$	$^{45}_{17}$Cl$_{28}$
$^{36}_{16}$S$_{20}$	$^{37}_{16}$S$_{21}$	$^{38}_{16}$S$_{22}$	$^{39}_{16}$S$_{23}$	$^{40}_{16}$S$_{24}$	$^{41}_{16}$S$_{25}$	$^{42}_{16}$S$_{26}$	$^{43}_{16}$S$_{27}$	$^{44}_{16}$S$_{28}$
$^{35}_{15}$P$_{20}$	$^{36}_{15}$P$_{21}$	$^{37}_{15}$P$_{22}$	$^{38}_{15}$P$_{23}$	$^{39}_{15}$P$_{24}$	$^{40}_{15}$P$_{25}$	$^{41}_{15}$P$_{26}$	$^{42}_{15}$P$_{27}$	$^{43}_{15}$P$_{28}$
$^{34}_{14}$Si$_{20}$	$^{35}_{14}$Si$_{21}$	$^{36}_{14}$Si$_{22}$	$^{37}_{14}$Si$_{23}$	$^{38}_{14}$Si$_{24}$	$^{39}_{14}$Si$_{25}$	$^{40}_{14}$Si$_{26}$	$^{41}_{14}$Si$_{27}$	$^{42}_{14}$Si$_{28}$
$^{33}_{13}$Al$_{20}$	$^{34}_{13}$Al$_{21}$	$^{35}_{13}$Al$_{22}$	$^{36}_{13}$Al$_{23}$	$^{37}_{13}$Al$_{24}$	$^{38}_{13}$Al$_{25}$	$^{39}_{13}$**Al**$_{26}$	$^{40}_{13}$**Al**$_{27}$	$^{41}_{13}$**Al**$_{28}$
$^{32}_{12}$Mg$_{20}$	$^{33}_{12}$Mg$_{21}$	$^{34}_{12}$Mg$_{22}$	$^{35}_{12}$Mg$_{23}$	$^{36}_{12}$Mg$_{24}$	$^{37}_{12}$Mg$_{25}$	$^{38}_{12}$Mg$_{26}$	$^{39}_{12}$Mg$_{27}$	$^{40}_{12}$Mg$_{28}$

- The intermediate isotopes of aluminum ($N \approx 28$) between predicted prolate and oblate ground state configurations

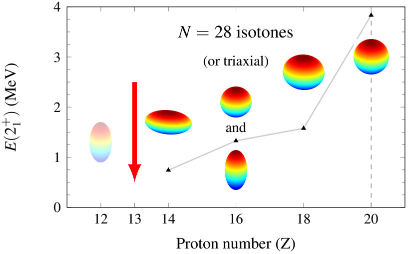

- Ex: observed with decreasing $E(2^+_1)$ energy
- Evolution of deformation from spherical ^{48}Ca $\rightarrow$ oblate ^{42}Si
- Removal of $\pi 0d_{3/2}$ protons $\Rightarrow \downarrow$ spiting of $\nu 0f_{5/2}$ and $\nu 0f_{7/2}$
- Jahn-Teller effect (near degeneracy of orbits) favours deformation
- $\Delta j = 2$ with occupied and valence proton/neutron orbitals $\Rightarrow$ cross-shell quadrupole excitations (SU(3) symmetries of Elliott)

Nucleon knockout reactions employed

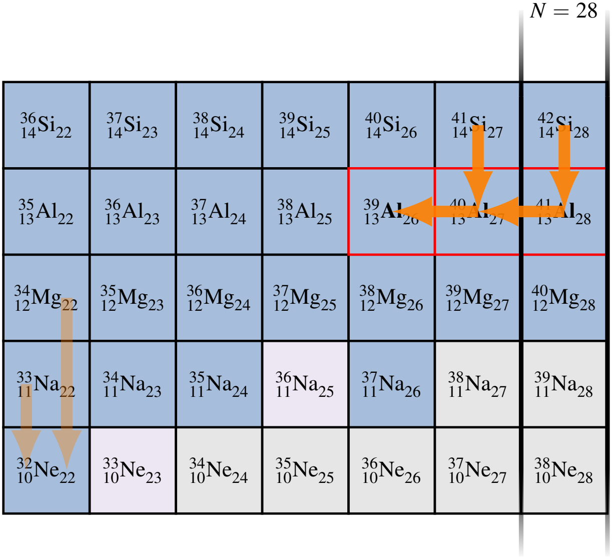

^{40}Al(C/C_2H_4,X)^{39}Al

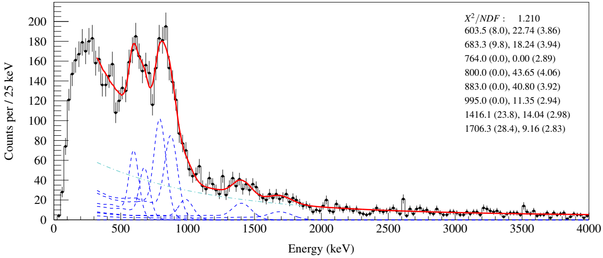

Fit of ^{40}Al(C/C_2H_4,X)^{39}Al doppler reconstructed γ-ray energy spectrum, $m_\gamma \leq 5$, and with add-back

E_γ (keV)	$\frac{\text{Yield}}{\text{100 ions}}$	Coinc.
$604(8)_{stat.}(5)_{syst.}$	14(2)	800
$683(10)_{stat.}(5)_{syst.}$	11(2)	883
764(8)[1,2]	0(3)[1]	
800(8)[2]	27(3)	604
883(8)[2]	25(2)	683
995(8)[2]	7(2)	883
$1416(24)_{stat.}(5)_{syst.}$	9(2)	
$1706(28)_{stat.}(5)_{syst.}$	6(2)	

[1] Not directly observed.
[2] Transition energy and uncertainty from literature Stroberg et al. 2014.

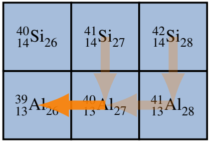

^{40}Al(C/C_2H_4,X)^{39}Al

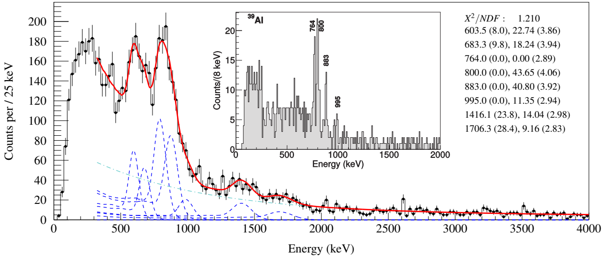

Fit of ^{40}Al(C/C_2H_4,X)^{39}Al doppler reconstructed γ-ray energy spectrum, $m_\gamma \leq 5$, and with add-back

E_γ (keV)	$\frac{\text{Yield}}{\text{100 ions}}$	Coinc.
$604(8)_{stat.}(5)_{syst.}$	14(2)	800
$683(10)_{stat.}(5)_{syst.}$	11(2)	883
764(8)[1,2]	0(3)[1]	
800(8)[2]	27(3)	604
883(8)[2]	25(2)	683
995(8)[2]	7(2)	883
$1416(24)_{stat.}(5)_{syst.}$	9(2)	
$1706(28)_{stat.}(5)_{syst.}$	6(2)	

1 Not directly observed.

2 Transition energy and uncertainty from literature Stroberg et al. 2014.

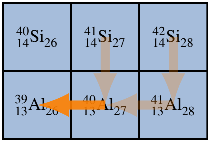

- New transitions in addition to previously observed 764(8), 800(8), 883(8) and 995(8) Stroberg et al. 2014

^{42}Si(C/C_2H_4,X)^{41}Al

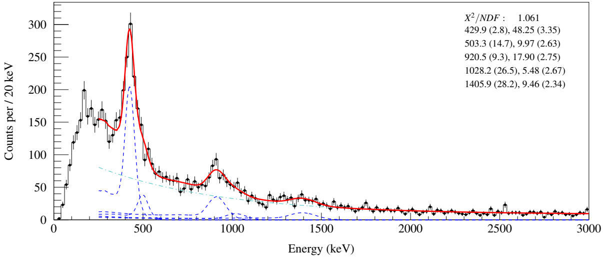

Fit of ^{42}Si(C/C_2H_4,X)^{41}Al doppler reconstructed γ-ray energy spectrum, $m_\gamma \leq 5$, and with add-back

E_γ (keV)	$\frac{\text{Yield}}{\text{100 ions}}$	Coinc.
$428(4)_{stat.}(5)_{syst.}$	12(1)	505
		923
$505(19)_{stat.}(5)_{syst.}$	2.7(9)	428
$923(10)_{stat.}(5)_{syst.}$	4.8(9)	428
$992(10)_{stat.}(5)_{syst.}$ [1]		
$1017(35)_{stat.}(5)_{syst.}$ [1]	1.3(9)	
$1424(27)_{stat.}(5)_{syst.}$	2.2(7)	

[1] The 992 keV transition fit from inelastic scattering and 1017 keV transition fit from proton knockout fall within uncertainties.

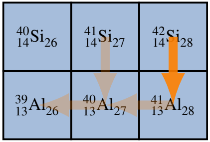

- All transitions observed for the first time

Tentative level schemes for ^{39}Al, ^{30}Al, ^{41}Al

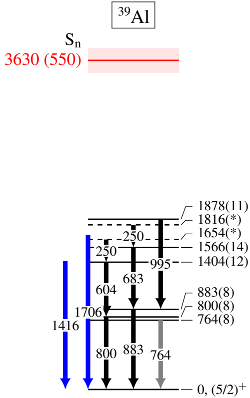

^{40}Al(C/C$_2$H$_4$,X)^{39}Al
^{39}Al(C/C$_2$H$_4$,γ)^{39}Al

Blue transitions from only singles spectra. Grey transition only from literature Stroberg et al. 2014.

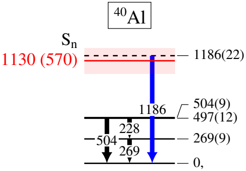

^{41}Al(C/C$_2$H$_4$,X)^{40}Al
^{41}Si(C/C$_2$H$_4$,X)^{40}Al
^{40}Al(C/C$_2$H$_4$,γ)^{40}Al

Blue transitions from only singles spectra.

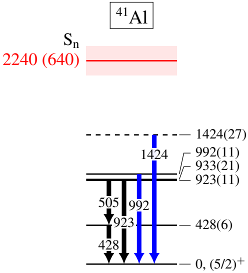

^{42}Si(C/C$_2$H$_4$,γ)^{41}Al
^{41}Al(C/C$_2$H$_4$,γ)^{41}Al

Blue transitions from only singles spectra.

^{39}Al Tentative experimental and shell model level scheme

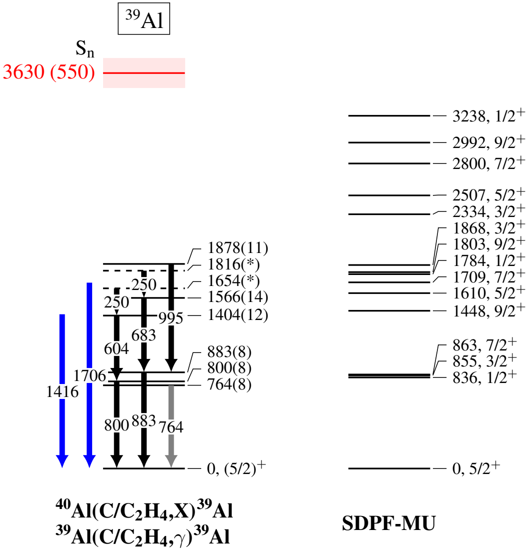

Blue transitions from only singles spectra. Grey transition only from literature Stroberg et al. 2014.

^{41}Al Tentative experimental and shell model level scheme

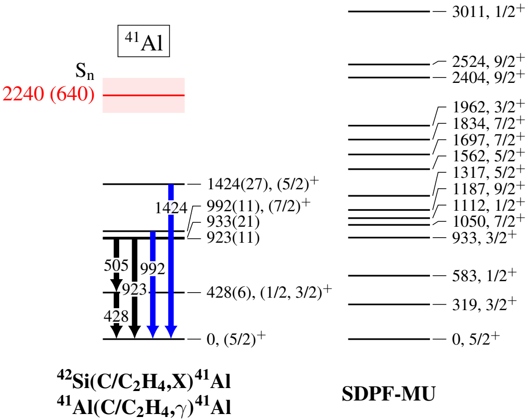

Blue transitions from only singles spectra

Odd-even ^{39}Al and ^{41}Al result summary

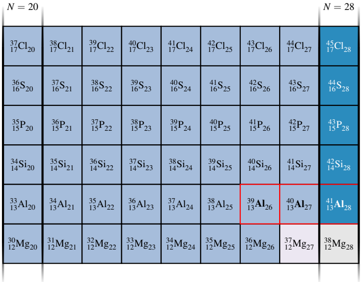

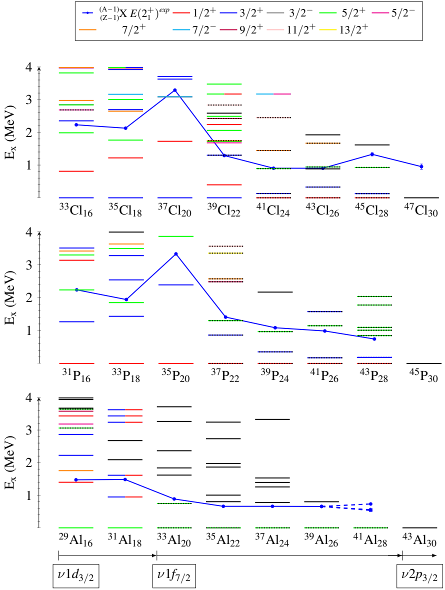

Odd-even ^{39}Al and ^{41}Al result summary

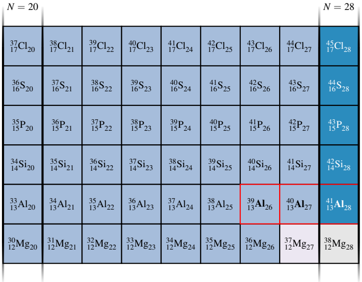

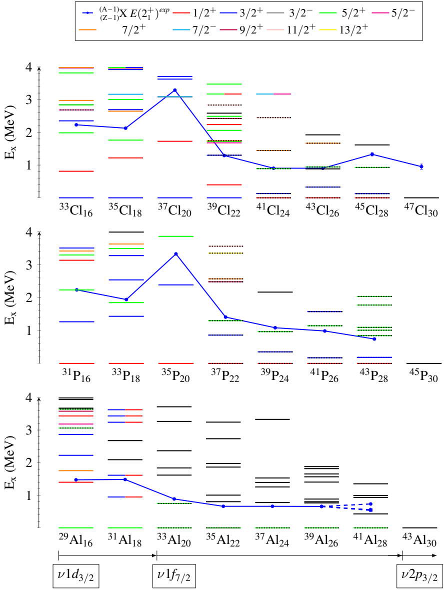

- New tentative excited states added for odd-even ^{39}Al and ^{41}Al
- Large drop (by half) in first excited state energy for ^{41}Al
- Fingerprint of the shell effect in odd-even levels? Level densities at magic numbers...

Odd-even ^{39}Al and ^{41}Al shell model result summary

- Similar features between experimental level scheme and shell model predictions for both odd-even ^{39}Al and ^{41}Al
- ^{39}Al and ^{41}Al predicted with prolate $\beta \approx 0.35$ ground states by SDPF-MU
- Similar ground state deformation to ^{38}Mg & ^{40}Mg?
- Only structural information on ^{40}Mg from inclusive two-proton knockout cross section $\Rightarrow$ suggests opposite configuration than ^{42}Si

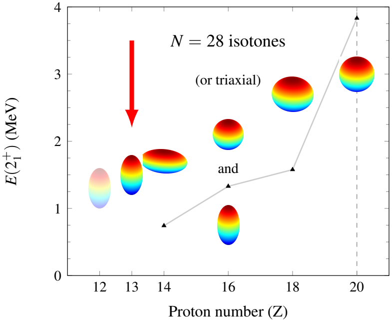

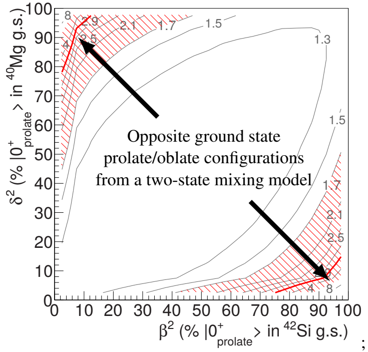

;

Percentage probabilities of prolate and oblate ground state wave-functions. Results from a two-state mixing model from experimental two-proton cross section. Figure from Crawford et al. 2014.

Mean field calculations and Nilsson model

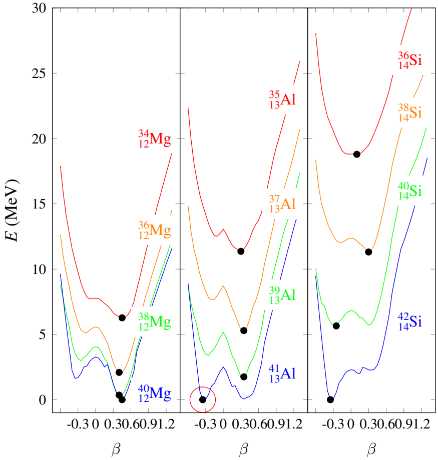

Hartree-Fock-Bogoliubov mean-field calculated energy surfaces with the D1S Gogny effective interaction Berger, Girod, and Gogny 1991 from the AMEDEE database Hilaire and Girod 2007. The surfaces of Mg, Al, Si are offset for visualization.

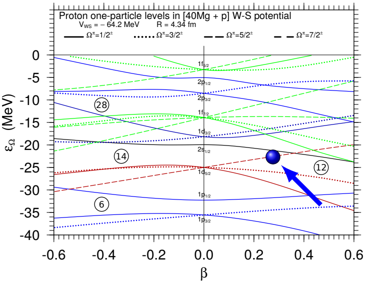

One-particle energies for protons of the $^{40}_{12}$Mg $\otimes\ \pi$ system as a function of axially symmetric quadrupole deformation with the Woods-Saxon potential.
I. Hamamoto private communication.

- Mean field calculation predicts ^{39}Al prolate $\beta \approx 0.35$ and ^{41}Al oblate $\beta \approx -0.35$
- Nilsson model suggests prolate for a ground state configuration of $5/2^+_{g.s.}$

Conclusion

- Large area of deformation investigated in neutron-rich $^{32}_{10}$Ne and $^{39-41}_{13}$Al

- First identification of $E(4_1^+)$ for $^{32}_{10}$Ne and confirmation of $E(2_1^+)$
  - Energy of $E(4_1^+)$ and ratio $R_{4/2}$ reproduced by state-of-the-art shell model calculations
  - Continued trend of deformation of $^{32}_{10}$Ne and confirmation of placement in *island of inversion*

- Contributions to knockout reaction cross section suppression ratios systematic trends

- New spectroscopic information of $^{39}_{13}$Al and first spectroscopy of $^{40}_{13}$Al and $^{41}_{13}$Al

- Tentative assignment of levels and agreement with shell model predictions ⇒ suggest prolate deformed ground states of $^{39}_{13}$Al and $^{41}_{13}$Al
  - Suggests loss of $N = 28$ spherical shell closure in $^{41}_{13}$Al
  - Might be a benchmark for theoretical predictions of ground state wave function (with near degenerate configurations)

^{32}Ne Experiment

I. Murray[1], M. MacCormick[1], D. Bazin[2], P. Doornenbal[3], N. Aoi[4], H. Baba[3], H. Crawford[5], P. Fallon[5], K. Li[3], J. Lee[6], M. Matsushita[3], T. Motobayashi[3], T. Otsuka[2 3 7], H. Sakurai[3 8], H. Scheit[9], D. Steppenbeck[3], S. Takeuchi[1], J. A. Tostevin[10], N. Tsunoda[7], Y. Utsuno[11], H. Wang[3], K. Yoneda[3]

^{39,40,41}Al Experiment

I. Murray[1], M. MacCormick[1], H. Crawford[5], P. Fallon[5], P. Doornenbal[3], D. S. Ahn[3], H. Baba[3], S. Bagchi[12], D. Bazin[2], K. Behr[12], F. Browne[3], S. Chen[3], M. L. Cortés[3], M. Cromaz[5], A. Estrade[13], N. Fukuda[3], H. Geissel[12], E. Haettner[12], M. Holl[14], M. Jones[5], N. Inabe[3], K. Itahashi[3], R. Kanungo[15], S. Kaur[16], S. Matsumoto[17], S. Momiya[8], T. Motobayashi[3], T. Nakamura[18], M. Niikura[8], S. Paschalis[19], M. Petri[19], A. Prochazka[12], H. Sakurai[3], C. Scheidenberger[12], Y. Shimizu[3], P. Schrock[7], D. Steppenbeck[3], M. Takechi[20], H. Takeda[7], S. Takeuchi[18], Y. Tanaka[12], R. Taniuchi[8], K. Wimmer[7], K. Yoshida[3]

[1]Institut de Physique Nucléaire, IN2P3-CNRS, Université Paris-Sud, Université Paris-Saclay, Orsay Cedex 91406, France
[2]National Superconducting Cyclotron Laboratory, Michigan State University, East Lansing, Michigan 48824, USA
[3]RIKEN Nishina Center, Wako, Saitama 351-0198, Japan
[4]Research Center for Nuclear Physics (RCNP), Osaka University, Ibaraki, Osaka 567-0047, Japan
[5]Nuclear Science Division, Lawrence Berkeley National Laboratory, Berkeley, United States
[6]The University of Hong Kong, Hong Kong
[7]Center for Nuclear Study (CNS), University of Tokyo, Wako-shi, Saitama 351-0198, Japan
[8]Department of Physics, University of Tokyo, 7-3-1 Hongo, Bunkyo, Tokyo 113-0033, Japan
[9]Technische Universität Darmstadt, Darmstadt 64289, Germany
[10]Department of Physics, University of Surrey, Guildford, Surrey GU2 7XH, United Kingdom
[11]Japan Atomic Energy Agency, Tokai, Ibaraki 319-1195, Japan
[12]GSI Helmholtzzentrum für Schwerionenforschung GmbH, 64291 Darmstadt, Germany
[13]Central Michigan University, Michigan, USA
[14]TRIUMF, Vancouver, Canada
[15]Saint Mary's University, Halifax, Nova Scotia, Canada
[16]Dalhousie University, Halifax, Nova Scotia, Canada
[17]Kyoto University, Kyoto, Japan
[18]Tokyo Institute of Technology, 2-12-1 O-Okayama, Meguro, Tokyo 152-8551, Japan [19]University of York, UK
[20]Niigata University, Niigata, Japan

Backup

^{40}Al Tentative experimental and shell model level scheme

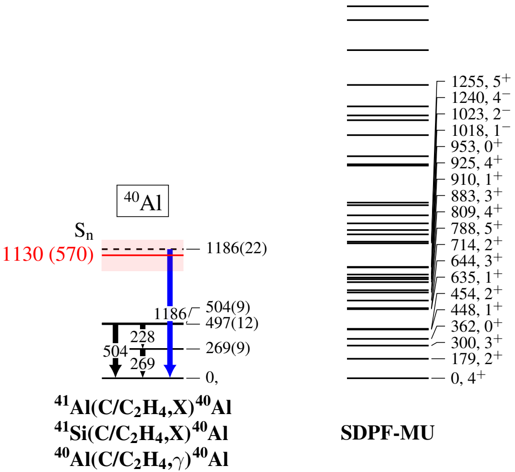

Odd-odd nuclei with high density of states

^{41}Si(C/C$_2$H$_4$,X)^{40}Al

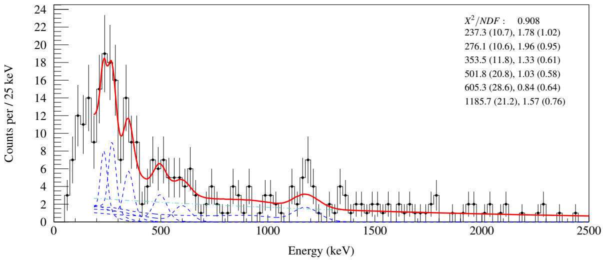

Fit of ^{41}Si(C/C$_2$H$_4$,X)^{40}Al doppler reconstructed γ-ray energy spectrum, $m_\gamma \leq 5$, and with add-back

E_γ (keV)	$\frac{\text{Yield}}{\text{100 ions}}$
$233(10)_{stat.}(5)_{syst.}$	12(5)
$276(10)_{stat.}(5)_{syst.}$	12(5)
$353(12)_{stat.}(5)_{syst.}$	7(3)
$516(32)_{stat.}(5)_{syst.}$	5(3)
$1186(21)_{stat.}(5)_{syst.}$	9(4)

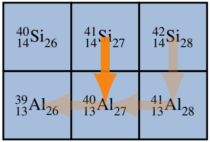

^{41}Al(C/C_2H_4,X)^{40}Al

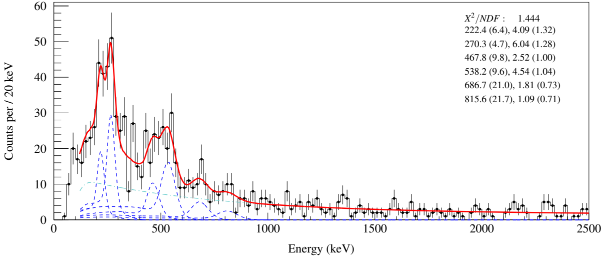

Fit of ^{41}Al(C/C_2H_4,X)^{40}Al doppler reconstructed γ-ray energy spectrum, $m_\gamma \leq 5$, and with add-back

E_γ (keV)	$\frac{\text{Yield}}{\text{100 ions}}$
$223(8)_{stat.}(5)_{syst.}$	12(4)
$270(5)_{stat.}(5)_{syst.}$	18(4)
$465(10)_{stat.}(5)_{syst.}$	7(3)
$532(10)_{stat.}(5)_{syst.}$	14(3)
$685(23)_{stat.}(5)_{syst.}$	5(2)

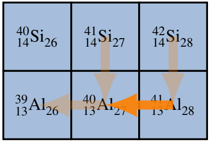

Detector array for low intensity radiation (DALI)

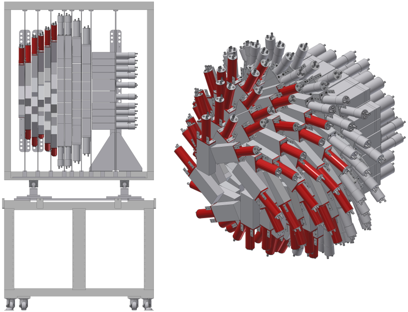

3D view of RIKEN DALI detector array

- 186 thallium-doped sodium iodine scintillator detectors
  - $\approx 25\%$ full energy peak efficiency for 1 MeV
  - $\approx 36\%$ with energy add-back procedure
- Energy add-back procedure:
  - Recover full energy of γ-rays when Compton scattered
  - Add detector responses within a given radius (15 cm)
  - Radius centered by highest energy response
- GEANT4-based simulation for DALI responses to fit exp. data
  - Input: individual detector energy resolution, state lifetime, target, beam velocity

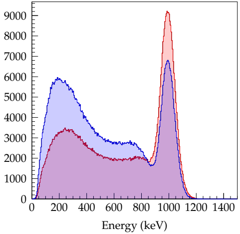

Ground state of ^{42}Si and ^{40}Mg

Cross section ratio,

$$R = \frac{\sigma_{44\to42}(0_1^+) + \sigma_{44\to42}(0_2^+)}{\sigma_{42\to40}(0_1^+)}$$

Wavefunctions,

$$\left|{}^{42}Si, 0_1^+\right\rangle = +\alpha\left|0^+; O\right\rangle + \beta\left|0^+; P\right\rangle$$

$$\left|{}^{42}Si, 0_2^+\right\rangle = -\beta\left|0^+; O\right\rangle + \alpha\left|0^+; P\right\rangle$$

f

$$\left|{}^{40}Mg, 0_1^+\right\rangle = \gamma\left|0^+; O\right\rangle + \delta\left|0^+; P\right\rangle$$

Two-nucleon amplitudes (from wave functions by projection of the Nilsson and BCS wave functions onto angular momentum state),

$$T_{44\to42}(0_1^+) = 0.35(\alpha T_{SO} + \beta T_{SP}) + 0.94(\alpha T_{PO} + \beta T_{PP})$$

$$T_{44\to42}(0_2^+) = 0.35(\alpha T_{SP} - \beta T_{SO}) + 0.94(\alpha T_{PP} - \beta T_{PO})$$

$$T_{42\to40}(0_1^+) = \alpha(\delta T_{OP} + \gamma T_{OO}) + \beta(\delta T_{PP} + \gamma T_{PO})$$

- With fixed quadrupole deformations of $|\beta_2| = 0.25, 0.35, 0.4$ for ^{44}S, ^{42}Si and ^{40}Mg
- Ground state wave-functions of ^{42}Si and ^{40}Mg must have opposite shapes

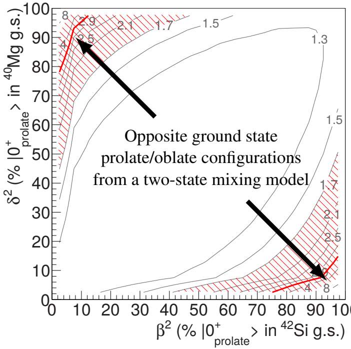

;

Percentage probabilities of prolate and oblate ground state wave-functions. Results from a two-state mixing model from experimental two-proton cross section. Figure from Crawford et al. 2014.

Eikonal reaction theory

- Sudden (adiabatic) approximation: the relative motion of the residue and knockout nucleon are assumed to be *frozen in time* during the collision (of the order of 1×10^{-23} s)
- Eikonal approximation (forward scattering): for two colliding bodies the wavefunction is unchanged in space, except for the vanishing portion within a cylinder of the overlap with an effective absorption radius
  - Spectator-core approximation: core (reaction residue) is assumed to not participate in dynamic excitation during the reaction

Stripping (inelastic breakup) cross section,

$$\sigma_{stripping} = \frac{1}{2j+1} \int d\vec{b} \sum_{m} \langle \psi_{jm} | \left(1 - |S_n|^2\right) |S_c|^2 | \psi_{jm} \rangle$$

where S_n and S_c are the elastic S-matrices of the systems of reaction residue and target, and removed nucleon and target, respectively. The diffraction process (elastic breakup) cross section,

$$\sigma_{diffraction} = \frac{1}{2j+1} \sum_{\sigma,m} \int d\vec{k} \int d\vec{b} \sum_{m} \left| \langle \psi_{\vec{k}\sigma} | (1 - S_n S_c) | \psi_{jm} \rangle \right|^2$$

Interpretation of two-nucleon knockout cross section - ^{34}Mg $\rightarrow$ ^{32}Ne

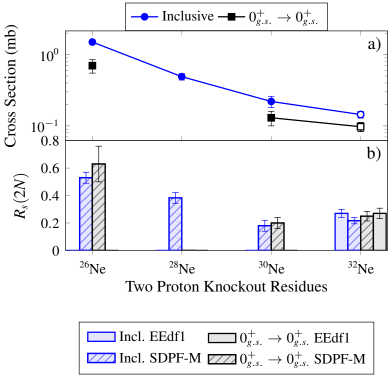

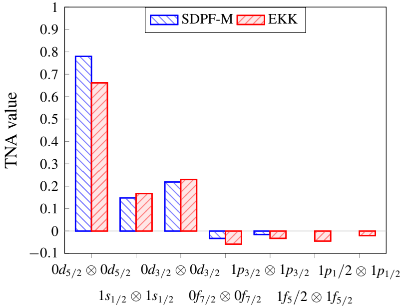

Data taken from Bazin et al. 2003; Fallon et al. 2010; Tostevin and Brown 2006

- Ratio of experimental to theoretical two-proton cross section additionally contributes to limited trend
- Similarity between shell model interactions related to similar two-nucleon amplitudes (TNAs)

Particle-hole probabilities

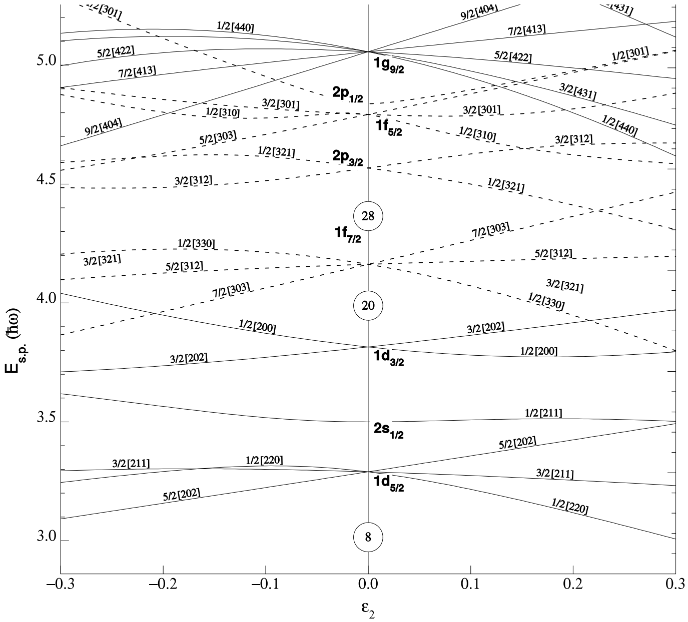

Nilsson Diagram

Table: ^{32,34}Mg and ^{30,32}Ne ground state neutron 0p-0h, 2p-2h and 4p-4h probabilties (%) calculated with the SDPF-M and EEDf1 interactions.

	SDPF-M			EEDf1		
	0p-0h	2p-2h	4p-4h	0p-0h	2p-2h	4p-4h
^{32}Mg	4.7	82.5	12.7	1.8	36.2	51.9
^{30}Ne	3.9	74.1	22.0	0.5	19.8	68.1
^{34}Mg	9.5	82.0	8.4	1.6	49.5	43.4
^{32}Ne	10.0	76.5	13.4	1.2	43.3	50.6

Exclusive experimental and theoretical cross sections

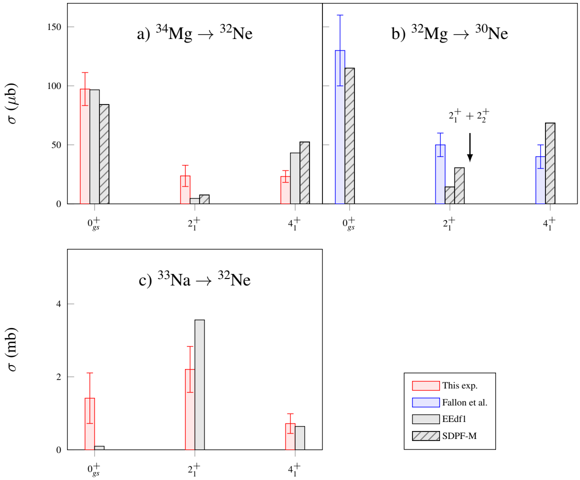

Experimental exclusive cross sections (σ) and theoretical predictions from shell model calculations. Exclusive theoretical cross sections are scaled by the inclusive R_s value for the visualization of the populated ratio. (a) Two-proton knockout reactions to $^{32}_{10}$Ne. (b) Two-proton knockout reactions to $^{30}_{10}$Ne Fallon et al. 2010. The cross section to 2^+_1 was conjectured to be unobserved feeding from a 2^+_2 state. The combined cross section is also plotted. (c) One-proton knockout reactions to $^{32}_{10}$Ne.